Wave absorber ballast optimization based on the analytical model for a pitching wave energy converter

Temiz, Irina; Ekweoba, Chisom; Thomas, Sarah; Kramer, Morten; Savin, Andrej

Published in:
Ocean Engineering

DOI (link to publication from Publisher):
10.1016/j.oceaneng.2021.109906

Publication date:
2021

Document Version
Publisher's PDF, also known as Version of record

Ocean Engineering 240 (2021) 109906

Contents lists available at ScienceDirect

Ocean Engineering

journal homepage: www.elsevier.com/locate/oceaneng

Wave absorber ballast optimization based on the analytical model for a pitching wave energy converter

Irina Temiz [a,*], Chisom Ekweoba [a], Sarah Thomas [b], Morten Kramer [b,c], Andrej Savin [a]

[a] Department of Electrical Engineering, Uppsala University Box 65, 75103 Uppsala, Sweden
[b] Floating Power Plant A/S, Park Alle 382, Vallensbæk, 2625, Denmark
[c] Department of the Built Environment, Aalborg University, Thomas Mann Vej 23, 9220 Aalborg, Denmark

ARTICLE INFO

Keywords:
Ballast optimization
Analytical model
Pitching wave energy converter
Power absorption performance

ABSTRACT

The present paper considers pitching wave energy converters (WECs) integrated in a floating platform, e.g., floating foundation for a wind turbine. Each WEC consists of a partially submerged wave absorber that rotates about the hinge located above the still water level under the influence of waves. Each wave absorber contains separated ballast tanks that are used to ensure the desired initial tilting angle of the absorber with respect to the floating foundation (called the rest angle). The same rest angle can be achieved by filling different ballast compartments that impacts the inertia moment about the hinge, response amplitude operator (RAO), resonance frequency of the absorber, and the power absorption performance. The exhaustive search for a suitable ballast configuration can quickly become a computationally expensive task depending on the number of ballast tanks. In this paper, the ballast optimization algorithm based on an analytical model is developed. The algorithm is applied to investigate the impact of the ballasts on the rest angle, RAO and resonance frequency of the wave absorber. It provides a base for ballast design and location for improved power absorption performance. The proposed algorithm can be adapted to the ballast optimization of other pitching WECs.

1. Introduction

The concept of ocean wave energy conversion to forms beneficial to humans dates as far back as 1799 (Clément et al., 2002). Since then, several technologies were invented to convert the kinetic and potential energy in waves into more useful forms such as electricity (Palme, 1920; Scott, 1965; Masuda et al., 1972). These inventions often faced challenges, such as efficiency and survivability, that could impede their viability in the energy market. Several reviews on wave energy converter technologies (Falnes, 2007; Falcão, 2010), economics (Astariz and Iglesias, 2015), sustainability (López et al., 2013) and their practicality (Drew et al., 2009) were done, where the common challenges encountered by these technologies were highlighted. Features such as efficiency and survivability need to be optimized to make wave energy converters (WECs) more competitive and viable, which led to several WEC geometry optimization studies (De Backer, 2009; Sjökvist et al., 2014; Kramer and Frigaard, 2002; Shadman et al., 2018).

An oscillating body can absorb more energy when operating at its natural frequency. Hence, for optimum wave energy absorption, a WEC should run close to its resonance frequency that is the same as the frequency of the incoming waves. Studies showed that a floating WEC whose motion was tuned to the characteristic frequency of the incident wave absorbed significantly more energy due to relatively high speed and amplitude when compared to devices working off-resonance (Falnes and Kurniawan, 2020; Budar and Falnes, 1975; Haraguchi and Asai, 2020). Frequency matching can be done actively through, e.g., latching and reactive control, or passively via adjusting the system's inertia using ballast tanks or tuned inertia mass. However, the actual waves are irregular and non-monochromatic, which poses a challenge in perfectly matching the device and wave frequencies.

Active WEC natural frequency tuning to match the predominant sea state was explored using different approaches such as reactive control (Yavuz et al., 2007), phase control through load control of a WEC (Falcão, 2008; Lopes et al., 2009), latching control of a single heaving point absorber (Saupe et al., 2014) and an array of point absorbing WECs (Thomas et al., 2018). The latching control strategy means holding the WEC at a fixed position and releasing it when the excitation force is maximum to achieve a synchronized motion with the wave. Implementation of the latching control requires knowledge of the future incoming wave in order to determine exact latching and unlatching time intervals. Therefore, a latching control technique that did not require prediction of waves and wave excitation forces was proposed in Lopes et al. (2009).

* Corresponding author.
E-mail address: Irina.Temiz@angstrom.uu.se (I. Temiz).

https://doi.org/10.1016/j.oceaneng.2021.109906
Received 4 March 2021; Received in revised form 13 September 2021; Accepted 21 September 2021
Available online 1 October 2021

Passive WEC natural frequency tuning was achieved by attaching another object with the neutral buoyancy to add the desired inertia to the WEC (Engström et al., 2009; Evans and Falcão, 2012). According to Haraguchi and Asai (2020), a notable increase of absorbed power was obtained when a tuned inertial mass, comprising of a tuning spring and a rotational mass, was attached to a point absorber; the absorbed power could be increased even more if the buoy was in resonance with the predominant wave frequency.

Another passive WEC control method is based on geometry optimization often complemented with inertia and mass optimization. In Vantorre et al. (2004), the buoy dimensions along with an external damping and supplementary inertia were considered as variable parameters to optimize the energy absorption of the WEC using linear frequency domain analysis and small scale experiments. A statistical analysis method known as "design of experiment" was utilized to optimize the dimension of a two-body point absorber in Soulard et al. (2009) and a one-body point absorber in Shadman et al. (2018). Improved wave energy absorption was achieved using shape optimization of the studied WECs in Babarit and Clement (2006), McCabe (2013), Goggins and Finnegan (2014).

The practice of using water-filled ballast tanks to modify the center of gravity and inertia properties of the WEC aiming to increase the energy absorbed from waves appeared to be promising. According to experimental results presented in Flocard and Finnigan (2012), Qiu et al. (2013), up to 70% increase in the capture factor using ballast water was recorded when operating in large regular waves. However, when there are many ballast compartments and, as a result, several possible combinations of filling the ballast tanks, the task of finding the optimum combination for the predominant wave frequencies becomes computationally expensive. In Colby et al. (2011), an evolutionary algorithm was proposed to optimize the ballast configuration of a WEC by generating a neural network to predict its power output with respect to geometric design variables and weight distribution. This approach resulted in reduced computational time by up to 99% and increased output power by 84% over ballast-free WEC.

In the present paper, the authors develop an analytical method to optimize the ballast combination and investigate the potential to improve power absorption of a WEC technology developed by Floating Power Plant[1] (FPP, see Fig. 1). FFP is the developer of a floating foundation for a wind turbine, in which wave energy converters (WECs) are integrated into the floating foundation. Each WEC consists of a partially submerged wave absorber and a power take-off (PTO) system located in a dry engine room far above the still water line (in the bridge). Under the influence of waves, the wave absorber rotates about the hinge located above the still water level. The PTO is a hydraulic oil system that applies a controlled force to the absorber to convert kinetic energy of the wave absorber to electrical power.

Each absorber contains several ballast tanks separated from each other. The ballast tanks can be filled with, for example, water to achieve a desired tilting angle of the absorber with respect to the floating foundation in calm water, from herein referred to as the rest angle. Conventionally, a particular configuration of ballast tanks is designed in CAD software; the inertia moment about the hinge is calculated for different combinations of filled ballasts, which is then used in hydrodynamic simulations. The procedure has to be repeated for a new configuration ballast tanks and new shape and dimensions of the wave absorber, which is time-consuming. Moreover, the searching procedure can become computationally expensive if the number of the ballast compartments is large.

In the present paper, a new approach to find the optimal ballast parameters is proposed. It relies only on the wave absorber design and the rest angle of the absorber. The procedure is independent of the shape of the ballast tanks or their placement inside the wave absorber and provides general guidelines for future design optimization, e.g., for power performance optimization studies including the floating platform dynamics. This study is based on the linear potential flow theory and the simulations are performed in frequency domain for simplicity, which is considered sufficient for the algorithm demonstration. Heras et al. (2019) showed that models based on the potential flow theory are able to capture the RAO and the resonance period of the wave absorber. Actual power performance optimization studies for the entire FPP platform with WECs is an upcoming study and will be performed in time domain.

Fig. 1. The hybrid wind-wave platform by Floating Power Plant. *Source:* Reproduced with permissions from Watson et al. (2019).

2. Mathematical model

2.1. Equation of motion

From the second Newton's law, the equation of the absorber motion is defined as follows:

$$I_{yy}\ddot{\theta} = M_g + M_b + M_h + M_r + M_e + M_o \tag{1}$$

where I_{yy} is the mass moment of inertia, $\ddot{\theta}$ is the angular acceleration of the body in pitch, M_g is the gravity moment, M_h is the hydrostatic moment, M_b is the buoyancy moment, M_r is the wave radiation moment, M_e is the wave excitation moment, and M_o is the moment due to other forces (for example, applied PTO forces, drag forces, mooring forces, etc.). All moments, the angular acceleration and the moment of inertia are calculated with respect to the y-axis (Fig. 2).

In this paper, we study the mass moment of inertia I_{yy} and its dependence on the ballast configuration. The response amplitude operator (RAO) obtained from (1) is used to demonstrate the impact of the ballast configuration on the resonance period and its RAO magnitude. Heras et al. (2019) showed that the resonance period of the absorber and the overall shape of the RAO curve remains the same for different models (wamit, linear, quasi-linear, and non-linear) and various other forces included in the equation of motion, though the RAO amplitude at the resonance and other periods is reduced when other moments are considered. Thus, the moments due to other forces are neglected in this study, and the equation of motion is limited to the linear hydrodynamic model when the absorber moves freely in the waves.

[1] www.floatingpowerplant.com

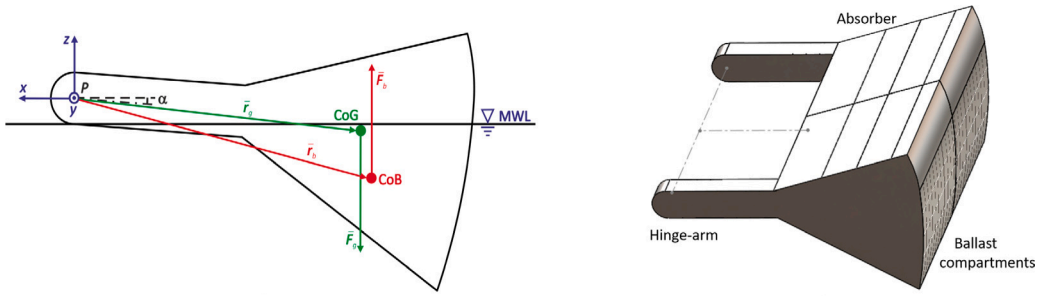

(a) (b)

Fig. 2. FPP wave absorber: (a) side view with coordinate system and forces; (b) CAD drawing with denoted parts. Here P is the pivot point and α is the rest angle.

Due to linearity, the equation of motion (1) can be solved in the frequency domain (Newman, 2017). Then the RAO of the absorber in pitch is defined by

$$H(j\omega) = \frac{\Theta}{A} = \frac{M_5(\beta)}{-\omega^2(I_{yy} + A_{55}) + j\omega B_{55}(\omega) + C_{55}} \tag{2}$$

where ω is the wave angular frequency, Θ is the absorber pitch motion in the frequency domain, A is the wave complex amplitude, $M_5(\beta)$ is the complex amplitude of the exciting moment in pitch for waves of direction β and unit amplitude, A_{55} and B_{55} are the frequency dependent added mass and radiation damping coefficients in pitch, C_{55} is the hydrostatic stiffness coefficient in pitch, and j is the complex unit ($j^2 = -1$).

The exciting moment, added mass, radiation damping, and the hydrostatic stiffness coefficients are found using a commercial boundary element method based software for fluid–structure interaction WAMIT (Wamit, 2013). For simplicity, we assume the absorber pitch motion in heading waves $\beta = 180°$.

From (2) it follows that larger I_{yy} correspond to longer resonance periods (equivalently, smaller angular resonance frequencies), and vice versa, smaller I_{yy} correspond to shorter resonance periods (equivalently, larger angular resonance frequencies).

2.2. Rest angle

The angle α between the xy-plane and the hinge-arm of the absorber is called the rest angle (Fig. 2a). If the absorber is at rest and there are no incoming waves, then the gravity and buoyancy moments cancel out each other $\vec{M}_g + \vec{M}_b = 0$, and the rest angle is constant.

The gravity moment arises due to the gravity force applied at the center of gravity (CoG) of the absorber when it rotates about the y-axis

$$\vec{M}_g = \vec{r}_g \times \vec{F}_g \tag{3}$$

where $\vec{r}_g = x_g\hat{x} + z_g\hat{z}$ is the position vector of the CoG, $\hat{x}$ and $\hat{z}$ are the unit vectors in the directions of the x and z axes respectively, and $\vec{F}_g$ is the gravity force. Executing the cross-product in (3), the gravity moment is equal to

$$\vec{M}_g = -mgx_g\hat{y} \tag{4}$$

where m is the absorber mass, and g is the gravitational acceleration magnitude.

Similarly, the buoyancy moment arises from the buoyancy force acting at the center of buoyancy (CoB) of the absorber when it rotates around the y-axis

$$\vec{M}_b = \vec{r}_b \times \vec{F}_b \tag{5}$$

where $\vec{r}_b = x_b\hat{x} + z_b\hat{z}$ is the position vector of the CoB, $\vec{F}_b = \nabla\rho_w g\hat{z}$ is the buoyancy force with submerged volume of the body ∇ and the water density ρ_w. From (5), the buoyancy moment is

$$\vec{M}_b = \nabla\rho_w g x_b\hat{y}. \tag{6}$$

From (6) and (4), it follows

$$mx_g = \nabla\rho_w x_b. \tag{7}$$

Note that the y-coordinates of the CoG and CoB are equal to zero because of the body symmetry with respect to the xz-plane. Moreover, for a given rest angle, the submerged part of the absorber remains the same; therefore, the submerged volume ∇ and the position vector $\vec{r}_b = x_b\hat{x} + z_b\hat{z}$ of the CoB are the same too. Here the position vector of the CoB is determined as the centroid of the xz-plane cross-section of the absorber submerged part. Thus, the right-hand side of Eq. (7) is constant, and the mass of the absorber is inversely proportional to the x-coordinate of the CoG, which potentially results in infinitely many solutions m and x_b of Eq. (7).

2.3. Center of gravity

Let us consider the absorber with a filled ballast. Since the absorber and the ballast filling do not intersect, from Eq. (A.2) it follows

$$m\vec{r}_g = m_a\vec{r}_{g,a} + m_b\vec{r}_{g,b} \tag{8}$$

where m_a, m_b and m are the masses of the absorber, ballast and their combination, respectively; analogously, $\vec{r}_{g,a} = x_{g,a}\hat{x} + z_{g,a}\hat{z}$, $\vec{r}_{g,b} = x_{g,b}\hat{x} + z_{g,b}\hat{z}$ and $\vec{r}_g = x_g\hat{x} + z_g\hat{z}$ are correspondingly the position vectors of the CoGs of the absorber, ballast and their combination. Hence, Eq. (8) can be written in the coordinate form:

$$mx_g = m_a x_{g,a} + m_b x_{g,b}, \tag{9}$$

$$mz_g = m_a z_{g,a} + m_b z_{g,b}. \tag{10}$$

Substituting (9) into (7) yields that the product $m_b x_{g,b}$ is constant:

$$m_b x_{g,b} = \nabla\rho_w x_b - m_a x_{g,a}, \tag{11}$$

It can be observed from (11) that a larger ballast mass m_b is required if the ballast is located closer to the pivot point.

2.4. Inertia moments

The hinge axis of the wave absorber is the y-axis in the reference frame shown in Fig. 2. If the absorber is rotated about the hinging point by an angle θ, the rotation matrix $R_y(\theta)$ is given by

$$R_y(\theta) = \begin{bmatrix} \cos\theta & 0 & \sin\theta \\ 0 & 1 & 0 \\ -\sin\theta & 0 & \cos\theta \end{bmatrix}. \tag{12}$$

It follows from (A.3) and (12) that the inertia moment I^*_{yy} remains unchanged if the absorber rotates around the y-axis by angle θ, i.e.

$$I'_{yy} = I^*_{yy}. \tag{13}$$

Another observation is made concerning the translation of the inertia moments. Let us consider a ballast placed along the y-axis from one hinge-arm to the other, and let us also, for simplicity, assume that

the principal axes of its inertia moments are parallel to the axes of the global coordinate system in Fig. 2. If the ballast filling CoG has coordinates $\vec{r}_{g,b} = x_{g,b}\hat{x} + z_{g,b}\hat{z}$ (the y-coordinate is zero due to the symmetry), then according to (A.4) and (A.5) the inertia moment I_{yy} of the ballast filling in the global coordinate system is equal to

$$I_{yy} = I^*_{yy} + m_b(x^2_{g,b} + z^2_{g,b}). \tag{14}$$

2.5. Power absorption

The method explained below is illustrated with an example of power absorption performance in irregular waves for different inertia moments. A moment due to a PTO force M_{pto} is included in the Eq. (1):

$$I_{yy}\ddot{\theta} = M_g + M_b + M_h + M_r + M_e + M_{pto}. \tag{15}$$

where the PTO moment is assumed to be linear, i.e. $M_{pto} = -B_{pto}\dot{\theta}$ with a constant PTO damping coefficient B_{pto}. The Eq. (15) can be rewritten in frequency domain:

$$[-\omega^2(I_{yy} + A_{55}) + j\omega(B_{55} + B_{pto}) + C_{55}]\Theta = AM_5(\beta). \tag{16}$$

Then the transfer function $H_{\theta,pto}$ of the absorber angular displacement with the PTO moment included is given by:

$$H_{\theta,pto}(j\omega) = \frac{\Theta}{A} = \frac{M_5(\beta)}{-\omega^2(I_{yy} + A_{55}) + j\omega(B_{55} + B_{pto}) + C_{55}} \tag{17}$$

and the transfer function $H_{\dot{\theta},pto}$ of the absorber angular velocity equals to

$$H_{\dot{\theta},pto}(j\omega) = j\omega H_{\theta,pto}(j\omega). \tag{18}$$

If an incident wave is regular, then the absorbed power can be found (Falnes, 2002) by

$$P(\omega) = 0.5B_{pto}\omega^2|\Theta|^2. \tag{19}$$

An irregular wave can be described by its wave spectrum $S_\zeta(\omega)$, then, according to Naess and Moan (2012), the response spectrum $S_{\dot{\theta}\dot{\theta}}(\omega)$ of the absorber angular velocity $\dot{\theta}$ is given by:

$$S_{\dot{\theta}\dot{\theta}}(\omega) = |H_{\dot{\theta},pto}(j\omega)|^2 S_\zeta(\omega) = \omega^2|H_{\theta,pto}(j\omega)|^2 S_\zeta(\omega). \tag{20}$$

Assuming a constant PTO damping coefficient B_{pto}, the average absorbed power for a given irregular wave is found by:

$$\bar{P}_a = B_{pto}\int_0^\infty S_{\dot{\theta}\dot{\theta}}d\omega = B_{pto}\int_0^\infty \omega^2|H_{\theta,pto}(j\omega)|^2 S_\zeta(\omega)d\omega. \tag{21}$$

3. Method

To formulate the optimization algorithm, additional simplifications and assumptions have to be made.

3.1. Cross-sectional ballast compartment arrangement

Let us consider an arrangement of the ballast compartments in the xz-plane as, for example, shown in Fig. 3a. The case when compartments A and B are filled with the same matter (Fig. 3a) is equivalent to presence of another bigger compartment $A + B$ marked in Fig. 3b in green whose CoG is located at CoG_{A+B} with mass $m_{A+B} = m_A + m_B$ and inertia moment $I_{yy}(A + B) = I_{yy}(A) + I_{yy}(B)$. It can be noted that the CoG of a combination of any number of the ballast compartments will be located inside the absorber, mass and inertia moment properties from above will be preserved as well. Particularly, the form of the compartment in the xz-plane is not important; any shape which gives the desired mass and moment of inertia can be used. Therefore, everywhere below the ballast compartments are rectangular cuboids.

It follows from (14), that the inertia moment with respect to the pivot point is dominated by the term $m_b(x^2_{g,b}+z^2_{g,b})$, because $x_{g,b}$ and $z_{g,b}$ are significantly greater than dimensions of the ballast compartment in the x and z directions. Nevertheless, the ballast compartment inertia with respect to the principal axis is taken into account when the inertia moment is calculated via Eq. (14).

3.2. Ballast compartment sizing

The method presented in the paper may refer to a matter of an arbitrary mass density. To make the method realistic and applicable to actual optimization studies, feasible ballast compartment sizing and CoG location are studied.

The ballast mass $m_b = \rho_b V_b = \rho_b l_{y,b} S_{xz,b}$, where ρ_b is the ballast matter, $l_{y,b}$ is the length of compartment in the y direction and $S_{xz,b}$ is the compartment area in the xz plane. Since the length of compartment $l_{y,b}$ is less than or equal to the length $l_{y,a}$ of the whole absorber in the y direction, then $m_b = \rho_b l_{y,b} S_{xz,b} \leqslant \rho_b l_{y,a} S_{xz,b}$ and

$$\frac{m_b}{\rho_b l_{y,a}} \leqslant S_{xz,b}. \tag{22}$$

From (22), the minimum ballast area $S^*_{xz,b}$ in the xz plane is

$$S^*_{xz,b} = \frac{m_b}{\rho_b l_{y,a}}. \tag{23}$$

Relation (23) also helps to determine possible locations $(x_{g,b}, z_{g,b})$ for the ballast CoG. In this paper, the ballast compartment is a rectangular cuboid and its cross-section in the xz-plane is a square. The whole compartment can be placed inside the absorber if its CoG $(x_{g,b}, z_{g,b})$ is located at the distance $d/2$ from each edge of the absorber cross-section in the xz plane, where d is the diagonal of the square.

$S^*_{xz,b}$ is not constant but changes depending on the ballast mass m_b as follows from (11). A larger area $S_{xz,b} > S^*_{xz,b}$ is possible if the length of the compartment $l_{y,b}$ is less than the length of the whole absorber $l_{y,a}$, but it is limited by the absorber area $S_{xz,a}$ in the xz-plane. However, a larger area $S_{xz,b}$ entails a greater distance from the ballast CoG to the absorber faces. Therefore, the case with a larger area $S_{xz,b}$ is equivalent to the case of another ballast with the area $S^*_{xg,b}$ with the same CoG.

3.3. Ballast compartment subdivision along the absorber width

Let us consider the case when a ballast compartment is split into several subdivisions along the length of the absorber in the y direction as in Fig. 4. To preserve the CoG on the absorber symmetry plane, i.e., the xz-plane, the subdivisions symmetrically placed with respect to the xz-plane are filled simultaneously. This is applied, for example, to subdivisions A and D, B and C in Fig. 4a, as well as to subdivisions A and C in Fig. 4b. Moreover, if subcompartments B and C in Fig. 4a should be filled simultaneously, then the case with four (even) number of subdivisions is equivalent in terms of mass, CoG, and inertia properties to the case with three (odd) number of subdivisions.

Now let us assume there is an odd number of subdivisions, for example, three as in Fig. 4b and the ballast subcompartment B and the whole compartment $A + B + C$ have the same projection on the xz-plane. Then their CoGs are the same, because their y coordinates are zero and the x and z coordinates are found as the centroid of the ballast compartment cross-section in the xz-plane. If the matter filling the ballast (sub)compartment is continuous and has a uniform mass density, then from the definition (A.1) the inertia moment $I^*_{yy}(B)$ of the subcompartment B about its principal axis is related to the inertia moment $I^*_{yy}(A + B + C)$ of the whole ballast compartment $A + B + C$ about its principal axis as their masses:

$$\frac{I^*_{yy}(B)}{I^*_{yy}(A + B + C)} = \frac{m_B}{m_{A+B+C}} \tag{24}$$

or, equivalently,

$$\frac{I^*_{yy}(B)}{I^*_{yy}(A + B + C)} = \frac{l_B}{l_{A+B+C}} = \frac{1}{k} \tag{25}$$

where l_B and l_{A+B+C} are respectively the lengths of B and $A + B + C$ along the y-axis, and k denotes the aspect ratio ($k > 1$).

If the subcompartment B is now replaced by a subcompartment B' with the CoG, matter density and mass $m_{B'}$ equal to the CoG, matter

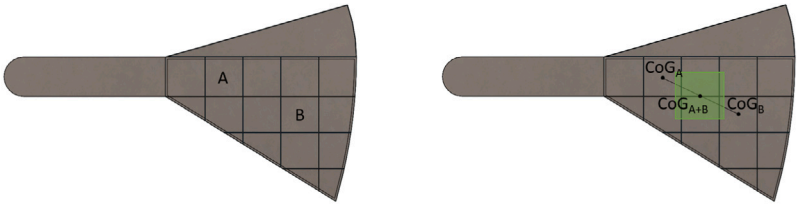

(a) (b)

Fig. 3. Side view of the FPP wave absorber with an example of cross-sectional ballast compartment arrangement: (a) two filled compartments marked; (b) equivalent single compartment (in green color). (For interpretation of the references to color in this figure legend, the reader is referred to the web version of this article.)

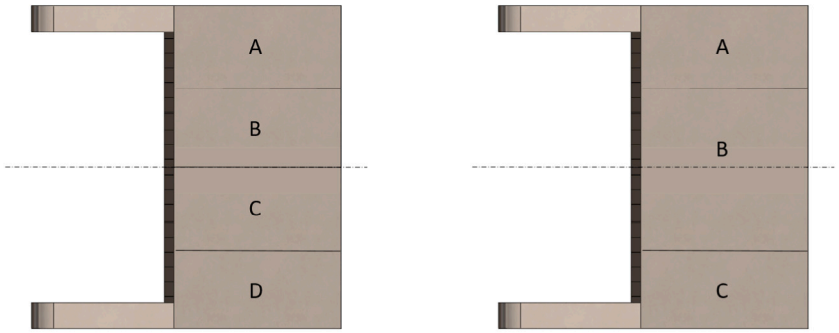

(a) (b)

Fig. 4. Top view of the FPP wave absorber with an example on ballast compartment subdivision along the absorber width: (a) even number of subcompartments; (b) odd number of subcompartments.

density and mass m_B of the subcompartment B, but whose length $l_{B'}$ is equal to l_{A+B+C}, then the cross-section area of the new compartment B' in the xz-plane should be scaled down by the factor k, and thereby, the inertia moment also becomes reduced by the same factor k when compared to the inertia moment $I^*_{yy}(B)$:

$$I^*_{yy}(B') = \frac{1}{k} I^*_{yy}(B) = \frac{1}{k^2} I^*_{yy}(A+B+C). \tag{26}$$

In this paper, the length of a ballast (sub)compartments is assumed to be equal to the length of the whole absorber along the y-axis, which can reduce the compartment inertia moment about its principal axis. However, since the contribution of the inertia moment about its principal axis is insignificant compared to the term $m_b(x^2_{g,b} + z^2_{g,b})$ in (14), the assumption introduces negligible error to the final results (see Section 4.4).

3.4. Algorithm

To summarize, ballast optimization is based on the following assumptions:

- The inertia moment I^*_{yy} of a ballast compartment does not change if the absorber is rotated about the y-axis;
- $m_b x_{g,b}$ for the ballast and mx_g for the combined absorber and ballast are constant;
- The matter of the same mass density is used across all ballast tanks;
- The ballast compartments continue through the entire width of the absorber;
- The ballast compartment cross-section in the xz-plane is a square of the area determined by the ballast mass m_b and its location;
- Changes in the mass properties of the empty absorber (e.g., due to re-arrangement of ballast separations) are negligible.

Then the optimization algorithm is formulated as follows:

1. Calculate mass properties of empty absorber;
2. Choose the rest angle α;
3. Calculate the possible ballast masses m_b for various horizontal locations $x_{g,b}$ of the ballast CoGs by Eq. (10);
4. Find the domain of the ballast CoG locations so that the whole ballast of the minimum area (23) can be placed inside the absorber;
5. Calculate the inertia moments $I_{yy,b}$ of the ballast compartments for various location $x_{g,b}$ and $z_{g,b}$ of the ballast CoGs by Eq. (14);
6. Obtain hydrostatic properties for given α: CoB, submerged volume;
7. Obtain hydrodynamic properties for given α in WAMIT: added mass, radiation damping, hydrostatic stiffness, excitation force;
8. Calculate the RAO for different ballast compartment locations and mass properties.
9. Choose the RAO (i.e., ballast location and mass properties) with required resonance frequency.

4. Results

The wave absorber shown in Fig. 2 is constructed in a CAD software SolidWorks©. A 3D CAD model of the wave absorber is made with material properties and dimensions matching the full-scale version of the absorber. The absorber ballast is divided into three main compartments along the width of the absorber, and each compartment is sub-divided into smaller ballast tanks. The compartments are separated by single thin walls. The model is then used to obtain the center of mass and inertia properties of the empty absorber, taken with respect to the pivot point as shown in Fig. 5. This model is also used for validation in Section 5. For convenience, the values everywhere below are dimensionless with the length scaling factor L equal to the total length of the absorber together with the hinge-arm in the x-direction. Everywhere in Section 4 the RAOs are calculated according to Eq. (2).

The wave absorber is titled with respect to the pivot point P by the rest angle, and the pivot point is above the calm water level, as shown in Fig. 5, where the rest angle is 4°. The purple area denotes the actual area for the possible ballast CoG locations for a chosen matter

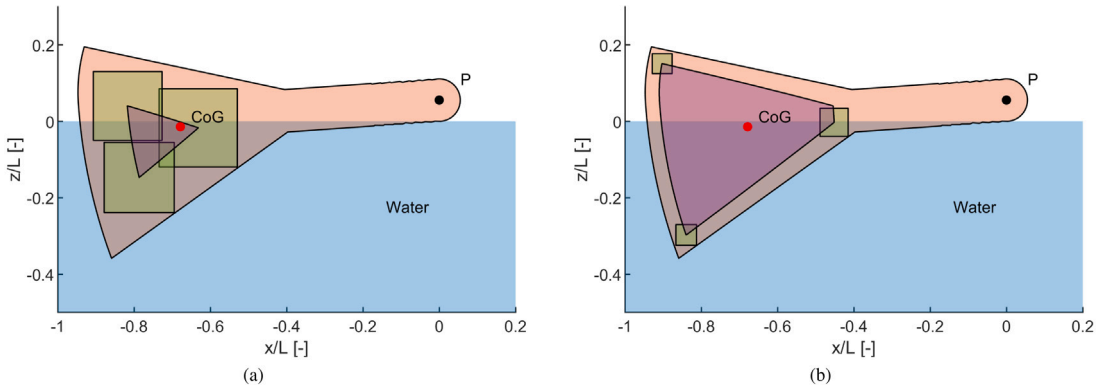

Fig. 5. Side view of the FPP wave absorber. The red area denotes the absorber; the purple area inside it denotes the area within which the ballast CoG can be located; the blue area denotes the calm sea water. Three green squares denote ballasts located at different locations; only one ballast is enough for the given rest angle. The red dot marks location of the empty absorber CoG; the black dot P is the pivot point. The scaling factor L is the total length of the absorber and its hinge-arm in the x-direction. Ballasts are found for: (a) a smaller matter mass density; (b) a larger matter mass density. (For interpretation of the references to color in this figure legend, the reader is referred to the web version of this article.)

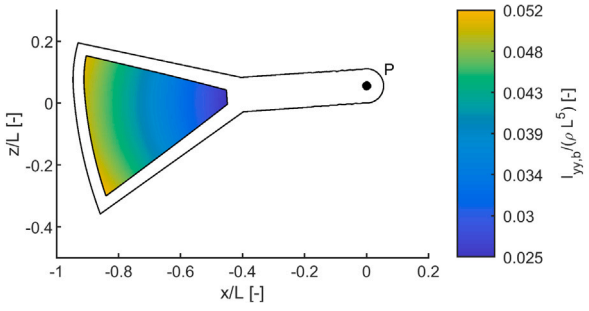

Fig. 6. Inertia moments of the ballast compartments at different locations of the absorber plotted as a function of the ballast CoGs.

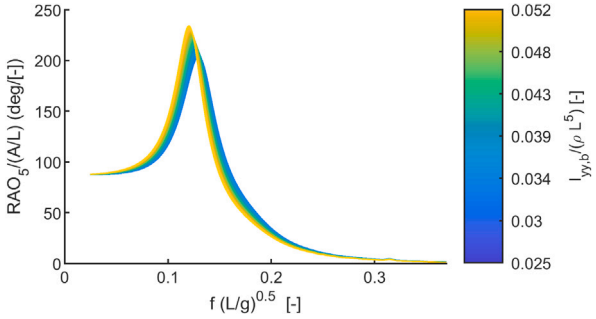

Fig. 7. Normalized RAO of the wave absorber in pitch for all possible values of the ballast inertia moments, where the RAO curves are color-coded by the ballast inertia moments. (For interpretation of the references to color in this figure legend, the reader is referred to the web version of this article.)

density. The green squares illustrate three equivalent ballast compartments: only one of these compartments is enough to achieve the rest angle of 4°. The impact of the matter mass density is demonstrated in Figs. 5(a) and 5(b): a greater matter density requires less ballast compartment size and results in a larger domain of the ballast CoG locations. Results below are presented for the matter mass density in Fig. 5b unless otherwise stated. It can also be noted that a larger ballast mass and, therefore, a larger ballast compartment is needed for the ballasts located closer to the pivot point P.

Following the optimization algorithm, the inertia moments of the ballast compartments (rectangular cuboids) are calculated for all combinations of the whole ballast mass m_b and the ballast CoG. The results are shown in Fig. 6. The inertia moments are increasing with increasing distance from the pivot point P, which is in line with Eq. (14) where I^*_{yy} is negligible (see Section 4.4).

In Fig. 7, the RAO curves for pitching absorber are plotted for all values of the ballast inertia moments. The resonance frequencies become lower with higher resonance response for greater (ballast) inertia moments. It is important to note that the pivot point P location and the rest angle are kept constant here. Thus, the wave absorber response can be changed by choosing different compartments to be filled with the same amount of matter, providing the balance between the gravity and buoyancy moments. However, the range of resonance frequencies is limited, which is further investigated in the sections below. Particularly, the impact of the ballast compartment dimensions, ballast matter, location of the pivot point P, and the rest angle is studied.

4.1. Impact of the ballast matter

In the previous section, a heavier ballast matter was chosen for illustration. The choice of the ballast matter is related to the size of the minimum ballast compartment as shown in Fig. 5: to maintain the rest angle a larger ballast compartment is needed for a lighter ballast matter. Fig. 8(a) and Fig. 8(b) show how the size and ballast matter density impact the ballast inertia $I_{yy,b}$, resonance frequency $f_{\text{res}}(L/g)^{0.5}$ and resonance response $\text{RAO}_5/(A/L)$. It can be observed that matter with greater matter mass density can slightly improve the range of the resonance frequencies and the absorber resonance response, which is related to how close the ballast compartments can be located to the wave absorber edge. In other words, smaller compartments corresponding to a greater ballast matter mass density can be placed closer or further away from the pivot point and, therefore, provide greater or less ballast inertia moment.

4.2. Impact of the pivot point position

In this section, the pivot point P vertical position is located 1.5 to 3 times higher compared with its initial location in the sections above, but the rest angle is kept the same, equal to 4°. The factors 1.5 to 3 are called the pivot point placement factors. The impact of changing the pivot point location on the ballast inertia moments, resonance frequencies, and resonance responses is shown in Figs. 9(a) and 9(b).

In Fig. 9(a), it can be noted that the varying range of the ballast inertia moments as well as the minimum and maximum values of the inertia moments are decreasing for higher located pivot points. It is

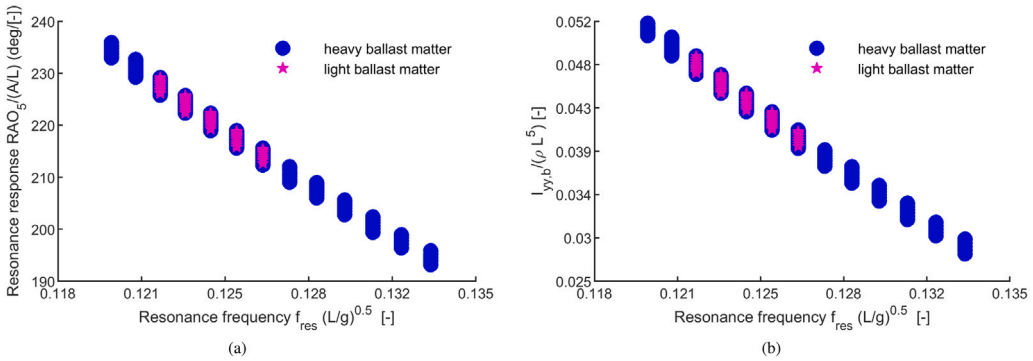

Fig. 8. Impact of heavier and lighter ballast matters: (a) resonance response $\mathrm{RAO}_5/(A/L)$ plotted with respect to resonance frequency $f_{\mathrm{res}}(L/g)^{0.5}$; (b) the ballast inertia moments $I_{yy,b}/(\rho L^5)$ plotted with respect to the resonance frequency $f_{\mathrm{res}}(L/g)^{0.5}$.

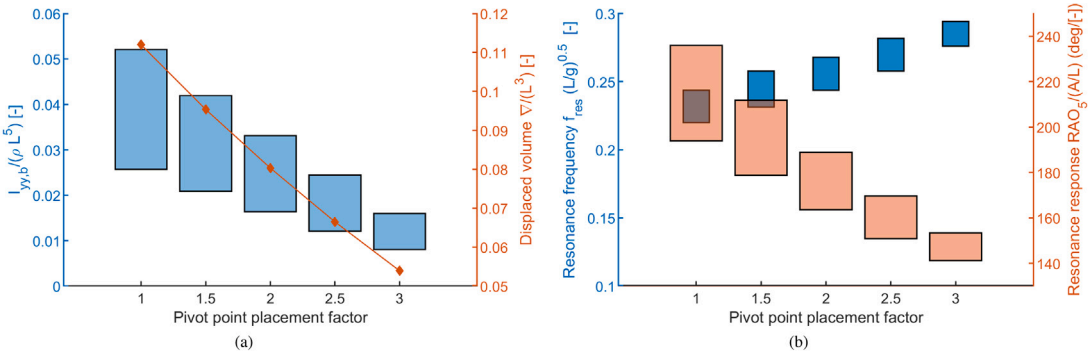

Fig. 9. Impact of the pivot point placement: (a) range of the ballast inertia moments (blue rectangles) and displaced volume of the wave absorber (red curve); (b) range of the resonance frequencies (blue rectangles) and the resonance responses in pitch (red rectangles). The horizontal axis presents the pivot point placement factors; factor 1 is used for the vertical distance from the calm water level to the pivot point location of the initial case. (For interpretation of the references to color in this figure legend, the reader is referred to the web version of this article.)

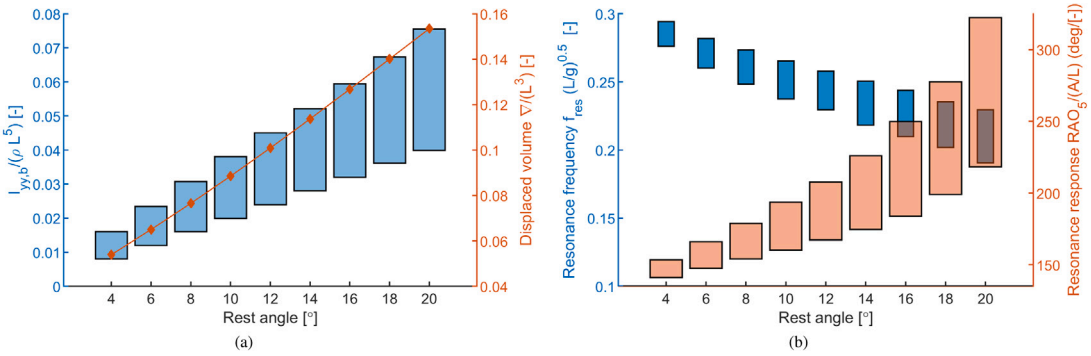

Fig. 10. Impact of the rest angle: (a) range of the ballast inertia moments (blue rectangles) and displaced volume of the wave absorber (red curve); (b) of the resonance frequencies (blue rectangles) and the resonance responses in pitch (red rectangles). The pivot point is placed three times higher than in the initial case. (For interpretation of the references to color in this figure legend, the reader is referred to the web version of this article.)

due to the reduced submerged volume of the absorber, which becomes nearly twice less if the pivot point is three times higher than the original placement. Fig. 9(b) demonstrates that when the displaced volume decreases almost double, the WEC resonance response (range, minimum and maximum values) is also reduced about two times. Moreover, the possibility to adjust the resonance frequency is also significantly lower.

4.3. Impact of the rest angle

In this section, the rest angle of the absorber varies from 4° to 20°, and the pivot point is located three times higher than in the initial case. This placement is chosen for illustration purposes: larger submerged volume variations are possible for different rest angles. The impact of the rest angle is shown in Figs. 10(a) and 10(b). As in the case with varying pivot point placement, the range of the ballast inertia moments are related to the displaced volume, affecting the range of the resonance frequencies and the corresponding resonance responses similarly.

4.4. Impact of the compartment size

The presented model is based on the assumption that the ballast length $l_{y,b}$ in the y-axis direction is equal to the absorber length $l_{y,a}$ in the same direction. According to (11), for a given ballast CoG location $(x_{g,b}, z_{g,b})$ the ballast mass m_b should be constant. Therefore, decrease of the ballast length $l_{y,b}$ compared to the absorber length $l_{y,a}$ should result in increase of the ballast cross-section area $S_{xz,b}$ compared to

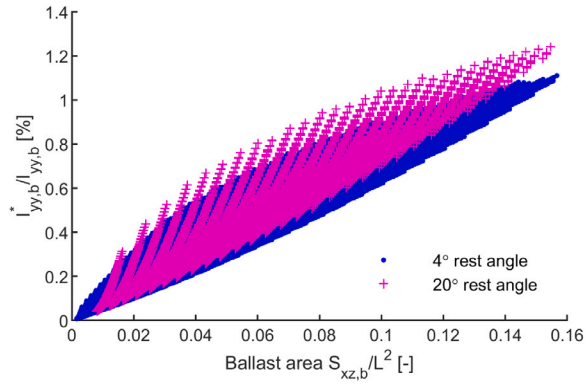

Fig. 11. Actual contribution of the ballast inertia moments $I^*_{yy,b}$ about the principal axis to the ballast inertia moments $I_{yy,b}$ about the pivot point plotted with respect to the ballast cross-section area $S_{xz,b}/L^2$.

the minimum ballast cross-section area $S^*_{xz,b}$ defined in (23). As it was discussed in Sections 3.2 and 3.3, this, in turn, impacts the ballast inertia moment about its principal axis $I^*_{yy,b}$. In this section, the actual impact of the ballast length and area to the ballast inertia moment with respect to the pivot point $I_{yy,b}$ is demonstrated.

Let us consider the case with the pivot point location three times higher than in the original case and the rest angles of 4° and 20°. The ballast inertia moments about the principal axis $I^*_{yy,b}$ relative to the ballast inertia moments $I_{yy,b}$ about the pivot point are compared in Fig. 11. It can be observed that the actual contribution of the ballast inertia moments $I^*_{yy,b}$ about the principal axis is less or equal to 1.4% of the ballast inertia moment $I_{yy,b}$ about the pivot point. Thus, the error associated with differences in the ballast length $l_{y,b}$ is negligible.

5. Validation with CAD model

In the previous sections, the potential to adjust the resonance period and response by means of filling a ballast compartment of the wave absorber has been studied. In this section, the mathematical model is validated against the CAD model for ballast compartments, as shown in Fig. 12, and the possibility to adjust the absorber response using water-filled ballasts is discussed.

Let us consider the particular ballast compartment subdivision (see Fig. 12). There is in total 19 subdivision in the cross-sectional plane (Fig. 12a) and three equal subdivision along the width of the absorber (Fig. 12b). However, the compartments along the bottom and aft of the absorber are substantially smaller than other compartments. Therefore different compartments have different contributions to the ballast mass and inertia moment. The subdivision along the width of the absorber allows for varying the ballast mass depending on how many compartments B, $A+C$, or $A+B+C$ are filled.

The total number of compartment combinations to fill in one subdivision (e.g. B) is equal to:

$$\sum_{k=0}^{N}\binom{N}{k} = (1+1)^N = 2^N. \tag{27}$$

In the considered example, $N = 19$, and the total number of combinations is $3 \cdot 2^{19} = O(10^6)$, that is too large to consider all combinations. Therefore, it is assumed that sea water is used to fill the ballast compartments, and they can be filled from the bottom, therefore, e.g., compartment 14 can be filled only when compartment 18 is filled. This reduces the number of combinations to 3240. Reducing the size of ballast compartments will increase the number of combinations to consider.

A CAD model-based ballast combination search, which uses the mass properties of the absorber and water (within each ballast compartment) obtained from SolidWorks©, is used to validate the analytical model. The moment of inertia and center of gravity are taken with respect to the pivot point. The pivot point placement used for the validation is at the location when the pivot point placement factor 3 is applied. For the different allowable combinations (with the constraint that a ballast compartment may only be filled if the ones below it in the same column are also filled), the combined masses, center of gravity, and inertia properties with respect to the rest angles are plotted together with the corresponding properties obtained from the mathematical model (Figs. 13(a)–13(d)).

Figs. 13(a) and 13(b) show the comparison between the analytical and CAD models for the achievable coordinates of the combined absorber and ballast CoGs. For the x-component, x_g, the results from CAD model agree well with the analytical model with the only difference that the CAD model allows for closer locations of the CoG to the pivot point. The z-components of the combined absorber and ballast CoGs, z_g, obtained from the analytical model, are partly located higher than the results from the CAD model. It is due to the filling approach chosen for the CAD model: the ballast compartments are filled from the bottom, while there is no restriction in the analytical model. When comparing the ballast masses from the CAD and analytical model (Fig. 13(c)), one can observe slightly larger ballast masses at greater rest angles, which can be explained by a closer horizontal placement of the CoGs to the pivot point. However, a more noticeable difference can be observed for the ballast inertia moments at greater rest angles (Fig. 13(d)). This difference is due to eventual numerical errors in the CAD software and further post-processing by the CAD model. This difference becomes especially noticeable for larger ballast masses.

6. Case study: power absorption performance

In this section, the application of the ballast optimization algorithm is illustrated by the case study on power absorption performance. The absorber with a pivot point placement factor of the pivot point placement of 3 and a rest angle of 20° is chosen. The results demonstrated in this section are not final, because only the wave absorber response is considered. The actual wave absorber motion and power absorption ability will be affected by the floating platform, in which the wave absorbers are integrated.

To ensure optimal power absorption, the PTO damping coefficient B_{pto} maximizing the absorbed power in regular waves given in (19) is found. It entails that for each inertia moment I_{yy}, the PTO damping coefficient B_{pto} depends only on wave frequency. The non-dimensional PTO damping coefficient for the chosen absorber placement is plotted in Fig. 14. In the simulation, the bounding values of B_{pto} for the parameter sweep are chosen to ensure that the maximum power P is reached for each wave frequency $f(L/g)^{0.5}$ and ballast inertia moment $I_{yy,b}$.

The irregular incident wave is assumed to have the JONSWAP spectrum with a peak enhancement factor $\gamma = 1.5$. The JONSWAP spectrum is obtained using the WAFO toolbox (Brodtkorb et al., 2000). Three different sea states with the same significant wave height H_s and different (equally spaced) energy periods T_e relevant for the North Sea are chosen. Sea state 1 (SS1) is selected so that its peak frequency is lower than the lowest possible absorber resonance frequency; sea state 3 (SS3) has its peak frequency higher than the highest possible absorber resonance frequency; and finally, the peak frequency of sea state 2 (SS2) lays within the possible resonance frequency range of the absorber. In this case, the available wave power density P_{irr} (see e.g. Falnes, 2002)

$$P_{irr} = \frac{\rho g^2}{64\pi} H_s^2 T_e \tag{28}$$

increases by the same amount between sea states, or, percent-wise, by 36.36% from SS1 to SS2 and by 26.67% from SS2 to SS3. The wave spectra for all three sea states and the dimensionless response amplitude operators of undamped absorber motion (Eq. (2)) for different ballast inertia moments are plotted in Fig. 15.

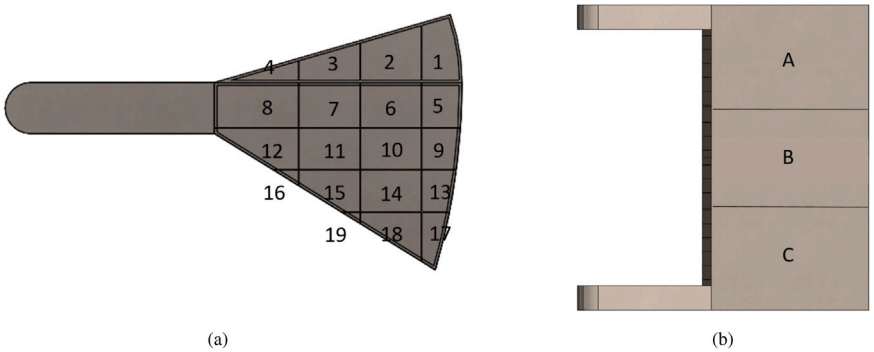

Fig. 12. CAD drawing of ballast compartment subdivision: (a) side view; (b) top view.

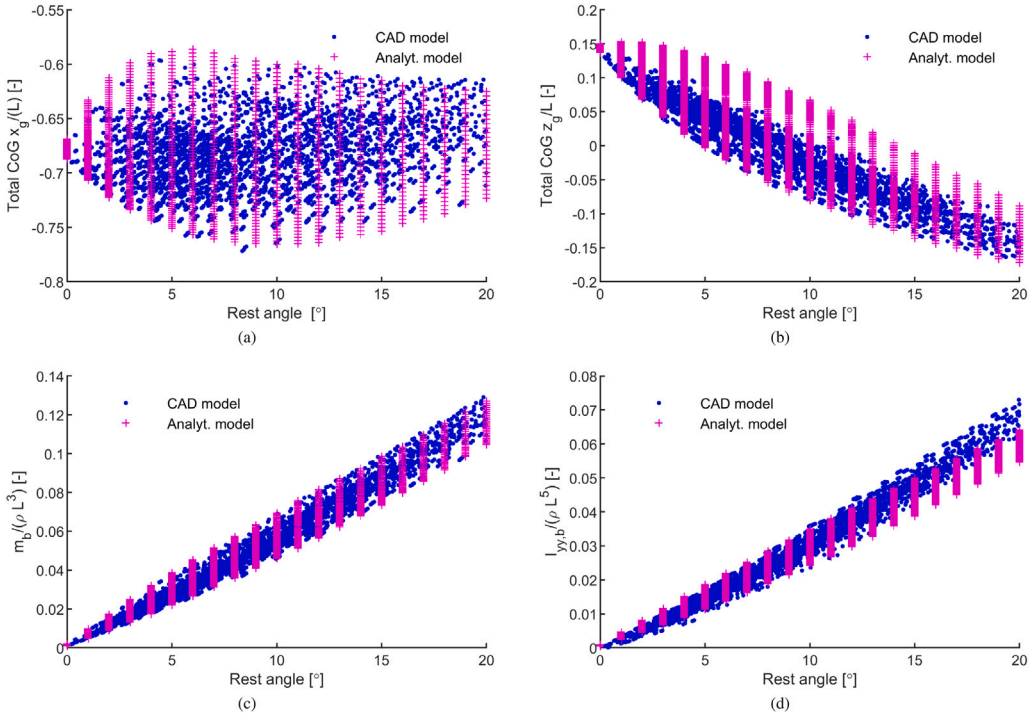

Fig. 13. Comparison of the absorber and ballast mass properties calculated based from the CAD and analytical methods plotted against different rest angles of the absorber: (a) the x-component of the combined absorber and ballast CoG; (a) the z-component of the combined absorber and ballast CoG; (c) the ballast mass $m_b/(\rho L^3)$; (d) the ballast inertia moment $I_{yy,b}/(\rho L^5)$.

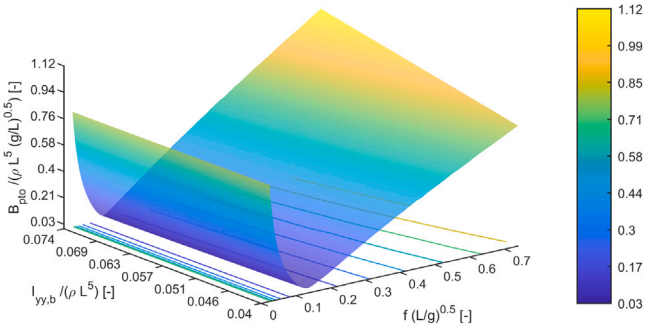

Fig. 14. Non-dimensional PTO damping coefficient $B_{pto}/(\rho L^5(g/L)^{0.5})$ plotted with respect to wave frequency $f(L/g)^{0.5}$ and the ballast inertia moment $I_{yy,b}/(\rho L^5)$.

The obtained average absorbed power with respect to different ballast inertia moments (solid lines) for all three sea states is plotted in Fig. 16. The dashed lines indicate the average values for corresponding sea states across all ballast inertia moments.

It can be observed that for SS2 the average absorbed power reaches its maximum for one of the ballast inertia moments within the ballast inertia moments interval. It occurs when the resonance frequency of the absorber coincides with the peak frequency of the sea state. For SS1 the average absorbed power increases with increasing ballast inertia moments, and for SS3 it is the opposite — the average absorbed power decreases with increasing ballast inertia moments. This can be explained that for larger (respectively, smaller) inertia moments the resonance frequency of the absorber becomes closer to the peak frequency of SS1 (respectively, SS3), although the resonance frequency significantly differs from the sea state peak frequency.

Another note can be made regarding the variability of the average absorbed power for the considered sea states and the potential to maximize the power absorption by adjusting the ballasts. The relative difference between the minimum and maximum values of the average absorbed power for various ballast inertia moments equals 35.9% for

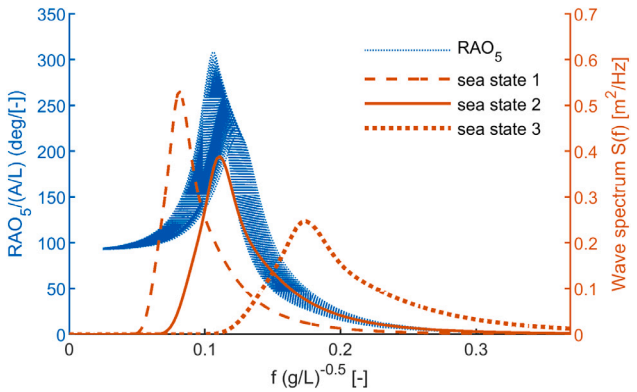

Fig. 15. Wave spectra for three sea states and normalized RAOs of undamped absorber motion for different ballast inertia moments.

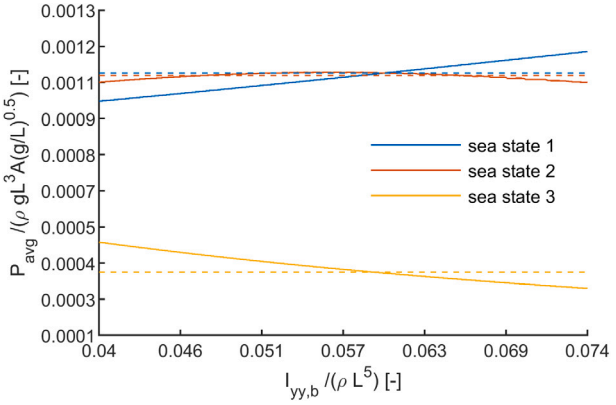

Fig. 16. Dimensionless average absorbed power plotted with respect to the ballast inertia moments for the three sea states. The solid lines correspond to the inertia dependent average absorbed power and the dashed lines denote the average values across all ballast inertia moments.

SS1, 3.5% for SS2, and 15.7% for SS3. It indicates that a substantial difference in power absorption by changing the ballast compartments can be made for sea states with the peak frequencies higher than the range of the resonance frequencies of the absorber. The impact of the ballast change is less (15.7%) for the sea states with peak frequencies lower than the range of the resonance frequencies of the absorber as for SS1. These adjustments are insignificant (3.5%) if the sea state peak frequencies are within the range of the possible resonance frequencies of the absorber as for SS2.

Comparing average values across all ballast inertia moments, it can be noted that the increase from SS1 to SS2 is almost 200% and from SS2 to SS3 it is less than 1%, which can be related to the differences in the respective RAOs for the bandwidth frequencies of the spectra. Although not all the available wave energy is absorbed in SS3, it may be preferable to have continuous power flow into the system with least variations between different sea states from the power system perspective. It suggests that the absorber ballast compartments should be designed so that the absorber efficiently operates at less energetic sea states. A similar (or slightly higher) power absorption will be possible in more energetic sea states. Fig. 17 shows that the RAO variations at zero frequency (or, equivalently, at longer waves) is insignificant for various combinations of rest angle, pivot point placement and ballast inertia moments.

7. Conclusions

In this paper, a new analytical approach to finding the optimal ballast combination for a pitching WEC has been proposed. The aim

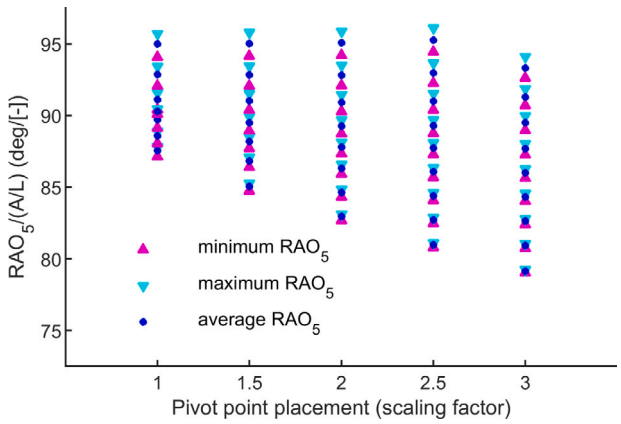

Fig. 17. Maximum, minimum and average values of RAOs at zero frequency for different pivot point locations and different rest angles. Extrema and average values are taken across various ballast inertia moments. Six points corresponding to lower pivot point placement and greater rest angle are excluded from the plot due to full submersion of the absorber and incomparable hydrodynamic performance.

was to investigate the potential to improve power absorption of the WEC technology using ballasts. The proposed method relies only on the wave absorber design and its rest angle. The algorithm is developed to quickly search the optimum ballast compartment combination; it will be applied for hydrodynamic optimization of the whole WEC. The search results in attainable inertia moments, resonance frequencies, and the absorber RAO for all possible ballast combinations.

The possibility to adjust the resonance frequency and response by means of filling ballast compartments of the wave absorber has been studied. The impacts of the compartment size, pivot point, and rest angle have also been investigated. Results have shown that the resonance frequencies become lower with higher resonance response for greater (ballast) inertia moments. It has also been observed that the inertia moments increase with increasing distance from the pivot point *P*. For varied rest angles, the range of the ballast inertia moments is related to the displaced volume, hence affecting the range of the resonance frequencies and the corresponding resonance responses.

Furthermore, using the JONSWAP spectrum, the power absorption performance with respect to different ballast inertia moments at three different sea states has been studied. The outcome indicates that a significant difference in absorbed power can be realized using ballasts for sea states whose peak periods are below the range of the resonance periods of the absorber. It can also be inferred from this investigation that the ballast compartments of the absorber should be designed in such a way that the absorber efficiently operates at less energetic sea states. Then a similar (slightly higher) power absorption could be possible in more energetic sea states.

The proposed analytical model for the ballast search has been validated using a CAD model. Results show reasonably good agreement between the CAD and analytical models. The algorithm presented in this paper can easily be extended to other pitching WEC concepts with different geometries, ballast shapes, and sizes.

CRediT authorship contribution statement

Irina Temiz: Conceptualization, Methodology, Software, Validation, Formal analysis, Investigation, Resources, Data curation, Writing - original draft, Writing - review & editing, Visualization, Supervision, Project administration, Funding acquisition. **Chisom Ekweoba:** Methodology, Software, Validation, Formal analysis, Data curation, Writing - original draft, Writing - review & editing. **Sarah Thomas:** Conceptualization, Methodology, Software, Resources, Writing - review & editing, Supervision. **Morten Kramer:** Methodology, Writing - review & editing. **Andrej Savin:** Methodology.

Declaration of competing interest

The authors declare that they have no known competing financial interests or personal relationships that could have appeared to influence the work reported in this paper.

Acknowledgments

This work was financially supported by Uppsala University, Sweden, STandUP for Energy, OESA project co-financed by the European Union under the European Regional Development Fund (ERDF) within the Interreg North Sea Region Programme 2015–2020 and Swedish Energy Agency (PA no. 48347-1).

Appendix A. Mass, CoG and inertia properties

A.1. Additivity of mass and inertia

The moment of inertia of a continuous body rotating about a specific axis P is calculated as follows

$$I_P = \iiint_V \rho_b(\vec{r})\vec{r}^2 dV \tag{A.1}$$

where $\vec{r}$ is the vector perpendicular to the axis P to a point of the body, and $\rho_b(\vec{r})$ is the mass density at this point.

It is well-known that the mass of a body and its inertia moment about a pivot P are additive. In other words, if the body consists of two and more non-intersecting parts, the mass and inertia moment about the pivot point of the whole body can be found as a sum of masses and inertia moments of its parts about the same pivot point.

A.2. CoG property

If a body consists of N non-intersecting parts with masses m_1, m_2, …, m_N and CoGs $\vec{r}_1$, $\vec{r}_2$, …, $\vec{r}_N$, then the mass m of the whole body and its CoG $\vec{r}$ is related to the parts' masses and CoGs via the following equation:

$$m\vec{r} = m_1\vec{r}_1 + m_2\vec{r}_2 + \cdots + m_N\vec{r}_N. \tag{A.2}$$

A.3. Rotation of the inertia matrix

If a reference frame $Oxyz$ is rotated about the origin O to a reference frame $Ox'y'z'$, then the inertia matrix I_P given in the former reference frame is transformed to the inertia matrix $I_{P'}$:

$$I_{P'} = S^T \cdot I_P \cdot S \tag{A.3}$$

where S defines rotation of $Oxyz$ to $Ox'y'z'$.

A.4. Translation of the inertia matrix

If a reference frame $Oxyz$ has axes parallel to the axes of a reference frame $O'xyz$ but with different origin O', then the inertia matrix I'_P in the reference frame $O'xyz$ can be found from the inertia matrix I_P given in the former reference frame by equation:

$$I_{P'} = I_P + I_t \tag{A.4}$$

where

$$I_t = m\begin{bmatrix} y_0^2 + z_0^2 & -x_0y_0 & -x_0z_0 \\ -x_0y_0 & x_0^2 + z_0^2 & -y_0z_0 \\ -x_0z_0 & -y_0z_0 & x_0^2 + y_0^2 \end{bmatrix}, \tag{A.5}$$

m is the mass of the body, and $\vec{r}_0 = \overrightarrow{OO'} = [x_0, y_0, z_0]$ is the position vector of the origin O' with respect to the reference frame $Oxyz$.

References

Astariz, S., Iglesias, G., 2015. The economics of wave energy: A review. Renew. Sustain. Energy Rev. 45, 397–408.

Babarit, A., Clement, A.H., 2006. Shape otimisation of the searev wave energy converter, in: Proc. 9th World Renewable Energy Congress, Florence, Italy.

Brodtkorb, P.A., Johannesson, P., Lindgren, G., Rychlik, I., Ryden, J., Sjö, E., et al., 2000. Wafo — a matlab toolbox for analysis of random waves and loads. In: Proc. 10'th Int. Offshore and Polar Eng. Conf., ISOPE, Seattle, USA. Vol. 3. pp. 343–350.

Budar, K., Falnes, J., 1975. A resonant point absorber of ocean-wave power. Nature 256 (5517), 478–479.

Clément, A., McCullen, P., Falcão, A., Fiorentino, A., Gardner, F., Hammarlund, K., Lemonis, G., Lewis, T., Nielsen, K., Petroncini, S., et al., 2002. Wave energy in europe: current status and perspectives. Renew. Sustain. Energy Rev. 6 (5), 405–431.

Colby, M.K., Nasroullahi, E.M., Tumer, K., 2011. Optimizing ballast design of wave energy converters using evolutionary algorithms, in: Proceedings of the 13th Annual Conference on Genetic and Evolutionary Computation Conference. GECCO '11. New York, NY, USA, 2011, pp. 1739–1746.

De Backer, G., 2009. Hydrodynamic Design Optimization of Wave Energy Converters Consisting of Heaving Point Absorbers. Department of Civil Engineering, Ghent University, Ghent, Belgium.

Drew, B., Plummer, A.R., Sahinkaya, M.N., 2009. A review of wave energy converter technology. J. Power Energy 223, 887–902.

Engström, J., Eriksson, M., Isberg, J., Leijon, M., 2009. Wave energy converter with enhanced amplitude response at frequencies coinciding with swedish west coast sea states by use of a supplementary submerged body. J. Appl. Phys. 106 (6), 064512.

Evans, D.V., Falcão, A.F.d.O., 2012. Hydrodynamics of Ocean Wave-Energy Utilization: IUTAM Symposium Lisbon/Portugal 1985. Springer Science & Business Media.

Falcão, A.F.d.O., 2008. Phase control through load control of oscillating-body wave energy converters with hydraulic pto system. Ocean Eng. 35 (3–4), 358–366.

Falcão, A.F.d.O., 2010. Wave energy utilization: A review of the technologies. Renew. Sustain. Energy Rev. 14 (3), 899–918.

Falnes, J., 2002. Ocean Waves and Oscillating Systems: Linear Interactions Including Wave-Energy Extraction. Cambridge University Press, UK.

Falnes, J., 2007. A review of wave-energy extraction. Mar. Struct. 20 (4), 185–201.

Falnes, J., Kurniawan, A., 2020. Ocean Waves and Oscillating Systems: Linear Interactions Including Wave-Energy Extraction. Vol. 8. Cambridge University Press.

Flocard, F., Finnigan, T., 2012. Increasing power capture of a wave energy device by inertia adjustment. Appl. Ocean Res. 34, 126–134.

Goggins, J., Finnegan, W., 2014. Shape optimisation of floating wave energy converters for a specified wave energy spectrum. Renew. Energy 71, 208–220.

Haraguchi, R., Asai, T., 2020. Enhanced power absorption of a point absorber wave energy converter using a tuned inertial mass. Energy 117740.

Heras, P., Thomas, S., Kramer, M., Kofoed, J.P., 2019. Numerical and experimental modelling of awave energy converter pitching in close proximity to a fixed structure. J. Mar. Sci. Eng. 7 (7), 1–27.

Kramer, M.V., Frigaard, P., 2002. Efficient wave energy amplification with wave reflectors. In: The Twelfth International Offshore and Polar Engineering Conference, Kitakyushu, Japan. International Society of Offshore and Polar Engineers, pp. ISOPE–I–02–108.

Lopes, M., Hals, J., Gomes, R., Moan, T., Gato, L., Falcão, A.d.O., 2009. Experimental and numerical investigation of non-predictive phase-control strategies for a point-absorbing wave energy converter. Ocean Eng. 36 (5), 386–402.

López, I., Andreu, J., Ceballos, S., De Alegría, I.M., Kortabarria, I., 2013. Review of wave energy technologies and the necessary power-equipment. Renew. Sustain. Energy Rev. 27, 413–434.

Masuda, Y., et al., 1972. Study of wave activated generator and future view as island power source, in: Proceedings of 2nd International Ocean Development Conference Preprints, Tokyo, Japan. Vol. 2, pp. 2064–2090.

McCabe, A., 2013. Constrained optimization of the shape of a wave energy collector by genetic algorithm. Renew. Energy 51, 274–284.

Naess, A., Moan, T., 2012. Stochastic Dynamics of Marine Structures. Cambridge University Press, Cambridge.

Newman, J.N., 2017. Marine Hydrodynamics, 40th Edition The MIT Press, Cambridge, MA.

Palme, A., 1920. Wave motion turbine. Power 52 (18), 200–201.

Qiu, S.-q., Ye, J.-w., Wang, D.-j., Liang, F.-l., 2013. Experimental study on a pendulum wave energy converter. China Ocean Eng. 27 (3), 359–368.

Saupe, F., Gilloteaux, J.-C., Bozonnet, P., Creff, Y., Tona, P., 2014. Latching control strategies for a heaving buoy wave energy generator in a random sea. IFAC Proc. Vol. 47 (3), 7710–7716.

Scott, K., 1965. Electricity from the wave. Sea Front. 11 (4), 202–207.

Shadman, M., Estefen, S.F., Rodriguez, C.A., Nogueira, I.C., 2018. A geometrical optimization method applied to a heaving point absorber wave energy converter. Renew. Energy 115, 533–546.

Sjökvist, L., Krishna, R., Rahm, M., Castellucci, V., Hagnestål, A., Leijon, M., 2014. On the optimization of point absorber buoys. J. Mar. Sci. Eng. 2 (2), 477–492.

Soulard, T., Alves, M., Sarmento, A., et al., 2009. Force reacting principle applied to a heave point absorber wave energy converter, in: The Nineteenth International Offshore and Polar Engineering Conference, Osaka, Japan. International Society of Offshore and Polar Engineers, pp. ISOPE–I–09–496.

Thomas, S., Eriksson, M., Göteman, M., Hann, M., Isberg, J., Engström, J., 2018. Experimental and numerical collaborative latching control of wave energy converter arrays. Energies 11 (11), 3036.

Vantorre, M., Banasiak, R., Verhoeven, R., 2004. Modelling of hydraulic performance and wave energy extraction by a point absorber in heave. Appl. Ocean Res. 26 (1–2), 61–72.

Wamit, 2013. User manual version 7.0. http://www.wamit.com/manual.htm.

Watson, S., Moro, A., Reis, V., Baniotopoulos, C., Barth, S., Bartoli, G., Bauer, F., Boelman, E., Bosse, D., Cherubini, A., Croce, A., Fagiano, L., Fontana, M., Gambier, A., Gkoumas, K., Golightly, C., Latour, M.I., Jamieson, P., Kaldellis, J., Macdonald, A., Murphy, J., Muskulus, M., Petrini, F., Pigolotti, L., Rasmussen, F., Schild, P., Schmehl, R., Stavridou, N., Tande, J., Taylor, N., Telsnig, T., Wiser, R., 2019. Future emerging technologies in the wind power sector: A European perspective. Renew. Sustain. Energy Rev. 113, 109270.

Yavuz, H., Stallard, T., McCabe, A., Aggidis, G.A., 2007. Time series analysis-based adaptive tuning techniques for a heaving wave energy converter in irregular seas. Proc. Inst. Mech. Eng., Part A: J. Power Energy 221 (1), 77–90.